Measurements of the structures of nanoparticles in flames by in situ detection of scattered x-ray radiation

Ossler, Frederik; Larsson, Jörgen

Published in:
Applied Physics Reviews

DOI:
10.1063/1.2140080

2005

Measurements of the structures of nanoparticles in flames by in situ detection of scattered x-ray radiation

Frederik Ossler and Jörgen Larsson

Citation: J. Appl. Phys. 98, 114317 (2005); doi: 10.1063/1.2140080
View online: http://dx.doi.org/10.1063/1.2140080
View Table of Contents: http://jap.aip.org/resource/1/JAPIAU/v98/i11
Published by the American Institute of Physics.

Measurements of the structures of nanoparticles in flames by *in situ* detection of scattered x-ray radiation

Frederik Ossler[a)]
Division of Combustion Physics, Lund Institute of Technology, P.O. Box 118, S-221 00 Lund, Sweden

Jörgen Larsson
Department of Physics, Lund Institute of Technology, P.O. Box 118, S-221 00, Lund, Sweden

(Received 6 June 2005; accepted 1 November 2005; published online 14 December 2005)

The angular pattern of scattered synchrotron x-ray radiation has been used to measure the composition of molecules and nanometer-sized particles in flames. The measured patterns were compared with patterns obtained from calculations for different species compositions. After ensuring that the calculations could reproduce the experiments for air and for ethylene flames under two different combustion conditions flames under special particle producing conditions were studied. In one case, the patterns showed a strong presence of spherical or fullerenelike structures with very little presence of graphitelike particles and little soot production on a cooling plate. In the other case, under soot producing conditions, the scattering showed a clear presence of nanometer-sized graphite particles. The results show that high concentrations of particles with the size around 1 nm can be produced in flames. These particles either remain free or condense into larger particles, depending on the combustion conditions. This technique opens up for experimental studies of molecular and particle dynamics in combustion processes and other processes where nucleation and structural transformations of particles occur. © *2005 American Institute of Physics*. [DOI: 10.1063/1.2140080]

INTRODUCTION

The increasing demand in the production of nanoparticles will require a deeper understanding of the physical and chemical mechanisms leading to particle formation. Techniques allowing measurements of particle properties *in situ* are then strongly desired. There is also the need to understand the impact that such particles may have on the environment and health. The environmental and health effects of carbon nanoparticles are being investigated.[1–4] The size distribution of nanoparticles from modern combustion sources have shown on different occasions a rather narrow peak in the concentration of particles of diameters, $D=1-3$ nm.[5–7] In this work we present an x-ray scattering method, which can be used to monitor such particles during combustion. Our main attention in this paper is drawn to particles smaller than 10 nm, which we will call nanoparticles. In particular, particles or structures smaller than 3 nm will be addressed.

The physical and chemical properties of the particles are strongly related to the size and structure. From an experimental point of view it is easier to obtain a high spatial resolution of the particles if they can be extracted locally from the reaction zone and then analyzed with high-resolution techniques *ex situ*. In the last few years there have been reports by different groups on the structures of nanometer-sized carbon particles extracted from different combustion sources and other high-temperature reactors. In these reports the high-resolution transmission electron microscopy (HRTEM) images[8–12] showed different nanostructures, such as diamond, graphitelike, fullerenelike caged structures, nanotubes, and glassy-carbon structures. In terms of atomic units, a high resolution in a broad mass spectrum can be obtained with mass spectrometric measurements. Samples from flames[6,13] and aerosols[14] have been studied with such techniques and information about the composition of different species such as fullerenes and polycyclic aromatic hydrocarbons (PAHs) were obtained.

In some situations, extraction procedures may alter the flow field and the temperature of the reaction zone which is being investigated. Such procedures can therefore strongly affect and interfere with the dynamics of particle formation, transformation, or destruction. Results from molecular-dynamics simulations[15–17] show that the dynamics of formation and transformations is strongly sensitive to the combustion temperature, with dynamic time scales from picoseconds to nanoseconds. Structures can therefore mutate rapidly with changes of flame conditions. In this respect *in situ* measurement techniques are preferred although they generally cannot allow optimal conditions of resolution. These techniques are complementary to the *ex situ* techniques since they can provide information on short-lived reactive species that may not survive through a sampling procedure.

Today only a few techniques are able to follow the dynamics of nanoparticles *in situ*, i.e., during the combustion process without interfering with the combustion processes itself. Laser-induced fluorescence (LIF) techniques are frequently used for the measurement of atomic and diatomic species, but become less effective for the study of polyatomic species and soot precursors such as PAHs. The main reason for the loss in efficiency is caused by the high temperatures that quench and spectrally broaden and shift the

[a)]Author to whom correspondence should be addressed; electronic mail: frederik.ossler@forbrf.lth.se

fluorescence spectra, which make the identification of PAH species more difficult. Reports on such studies can be found in different references.[18–22] LIF techniques can be used for studying characteristic sizes of PAH in combustion environment, taking into account the influence of temperature and oxygen quenching.[22,23] One may calibrate the quenching dependence of a particular species to temperature and oxygen concentration. The species can then be used as a dopant or a probe molecule to measure temperature and fuel equivalence ratio in combustion related experiments.[22,24–26]

The laser techniques so far that to some extent have been able to characterize nanoparticles *in situ* are based on laser scattering/extinction[27,28] (LSE) and laser-induced incandescence (LII).[29,30] The information obtained from LSE is the characteristic size and optical properties of the particles. However, details about the size distribution function and particle structure are more difficult to obtain with these techniques. LII has been generally used for measurements of soot-volume fractions and for information on the primary particle size of soot.[23] Techniques based on cavity ring down may be used to measure very low concentrations of soot particles down to concentrations of 0.1 ppb for soot-volume fractions.[31]

In order to resolve the structure and the size of nanometer-sized particles the wavelength of the scattering process should be of the order of the interatomic bond distance, which typically is 1–2 Å and therefore far more powerful than laser scattering techniques. Synchrotron x-ray scattering based on small-angle x-ray scattering[32–34] (SAXS) and wide-angle x-ray scattering[35] (WAXS) in this wavelength region have been used for measurements of nanoparticles or soot particles. Soot properties have also been investigated, at synchrotron radiation facilities, by measuring the x-ray induced ionization current from flames.[36] Neutrons, which have different scattering properties than x-ray photons, have also been used for studying soot particles in the small-angle neutron scattering (SANS) region.[37] Among these techniques we will further discuss the possibilities of SAXS and WAXS below.

SAXS techniques are useful to measure the size distribution of ultrafine particles in the size range between 1 and 100 nm in atmospheric pressure flames.[32,33] SAXS has also been used to measure the synthesis of silica nanoparticles in flames.[34]

Whereas the highest sensitive to particle diameter is observed in the small-angle region, the wide-angle region contains mostly information on particle structure. WAXS measurements may thus provide with complementary information on particles. The report on WAXS measurements on flames showed how the scattering patterns in the wide-angle region change with the conditions inside the flame:[35] Signatures changed from fullerenelike scattering structures to graphiticlike structures in the subnanometer and nanometer length scale, respectively.

In this work we report in more detail how the WAXS signals are related to structures and composition of the flame. We classify different signatures in the scattering signal and relate them to structural properties of nanoparticles. The basis for the comparison are scattering calculations for different types of nanoparticles and molecules and some characteristic scattering patterns that have been measured for air and flames.

THEORY

Several textbooks treat the subject of x-ray scattering[38–40] and scattering of electromagnetic radiation in general.[41–43] In this section we summarize the most important parts that are needed for experimental applications of x-ray scattering. We are particularly interested in scattering properties of different species for photon energies between 5 keV (2.48 Å) and 10 keV (1.24 Å). We take the polarization of the x-ray wave into account in the scattering simulations, since most synchrotron x-ray facilities produce polarized radiation. In this range of photon energy, the three major processes of interaction are photoionization, coherent scattering, and incoherent scattering, often referred to as Compton scattering.

The number of photons $dP_i(\theta,\varphi)/d\Omega$ scattered by an object (i), per time unit and unit of the solid angle can be described as

$$\frac{dP_i(\theta,\varphi)}{d\Omega} = \frac{d\sigma_i(\theta,\varphi)}{d\Omega} I_0, \tag{1}$$

where $d\sigma_i(\theta,\varphi)/d\Omega$ is the differential cross section, θ and φ are the scattering angle in the plane of scattering and the azimuth angle (between the scattering plane and the plane of polarization), respectively. I_0 is the irradiance (W m^{-2} s^{-1}) of the source.

In the energy region of interest, the cross section for x-ray scattering is defined as

$$\sigma_i(\theta,\varphi) = \sigma_{i,\mathrm{Coh}}(\theta,\varphi) + \sigma_{i,\mathrm{Incoh}}(\theta,\varphi), \tag{2}$$

where $\sigma_{i,\mathrm{Coh}}(\theta,\varphi)$ and $\sigma_{i,\mathrm{Incoh}}(\theta,\varphi)$ are the coherent and incoherent-scattering cross sections.

Whereas the main cause for attenuation of radiation in a medium is caused by photoionization. The attenuation is given by

$$I(l) = I_0 \exp(-\mu l) = I_0 \exp(-\sigma_{\mathrm{tot}} N l), \tag{3}$$

σ_{tot} is determined by the the photoionization cross section, μ is the attenuation coefficient, N is the total concentration of species, and l is the path lengths of the radiation in the medium. The values of μ can be obtained from tabulated values of the mass attenuation coefficients μ/ρ, where ρ is density of the medium.[44] For a composition $\mu/\rho = \Sigma_i w_i(\mu/\rho)_i$, where w_i is the fraction by weight of species i.

Coherent scattering shows distinct polarization properties, given by the Rayleigh theory[41] of scattering. For linearly polarized radiation it is convenient to define two polarization components: one orthogonal (s) to the plane of scattering and the other parallel (p) to the plane of scattering.[42] One can then define the irradiation of the incident radiation in the following way:

$$I_{p0} = I_0 \cos^2(\varphi), \quad I_{s0} = I_0 \sin^2(\varphi), \tag{4}$$

where φ is the angle between the plane of polarization of the incident radiation and the plane of scattering. For a free elec-

tron i one obtains the scattering cross section for orthogonally polarized radiation,

$$\frac{d\sigma_{si}(\theta,\varphi)}{d\Omega} = \frac{e^4}{{m_e}^2 c^4} = {r_e}^2, \tag{5}$$

which is known as Thomson scattering, where r_e is the classical electron radius 2.818×10^{-15} m. An important parameter used to describe scattering is the exchange of momentum, q,

$$q = \frac{4\pi}{\lambda}\sin\left(\frac{\theta}{2}\right). \tag{6}$$

However, sometimes in the literature and tables the parameter for the exchange of the momentum is given as $q/4\pi$. One should notice also that the assignment "θ" frequently corresponds to half the scattering angle. For historical reasons the scattering equations in textbooks are often defined for unpolarized radiation and therefore often contain a factor that can be traced to $[1+\cos^2(\theta)]/2$.

In order to calculate the coherent scattering from an object we divide it into a number of small unit volumes. The coherent scattering from an object, where the incident and scattered photons have the same energy, can be regarded as the result from the superposition of the scattered electric complex field amplitudes from each unit volume. Thus the units of volume scatter independently of each other in accordance with the Rayleigh-Gans theory known from optical scattering theory.[41] We can assign a density, a distribution of electric dipoles, or the electric dipole moment to the object and then calculate the superimposed sum of electric fields from each volume unit, for any direction in the space, i.e., θ and φ. The θ-dependence depends on the individual phases at the point of superposition, and the polarization dependence is given by the φ-dependence which can be separated into one term,

$$\frac{dP(\theta,\varphi)}{d\Omega} = \frac{dP(\theta,\varphi=\pi/2)}{d\Omega}[\cos^2(\theta)\cos^2(\varphi)+\sin^2(\varphi)]. \tag{7}$$

The resulting angular (θ) distribution of the scattered radiation depends on the electron-density distribution of the object.

$$dP_s(q) = \left| r_e Z\int_V \rho(\bar{r}-\overline{r_0})\exp[-i\bar{q}(\bar{r}-\overline{r_0})]dV\right|^2 I_{s0}d\Omega, \tag{8}$$

$$dP_s(q) = {r_e}^2 {N_e}^2 A(q) I_{s0} d\Omega, \tag{9}$$

in units of electrons Eq. (9) becomes

$$dP_s(q) = {N_e}^2 A(q) I_{s0} d\Omega, \tag{10}$$

where q is the exchange of momentum during the scattering. $Z=N_e$ is the total number of electrons present in the object. $A(q)$ is the absolute squared of the calculated volume integral.

The integrals $f=Z\int_v \rho(\bar{r}-\overline{r_0})\exp[-i\bar{q}(\bar{r}-\overline{r_0})]dV$ have been calculated for different atoms and are known as atomic form factors and have been tabulated.[45,46] These factors are used to calculate the differential cross sections for crystals and molecules.

The incoherent scattering from a free electron is described by Compton scattering. The photon looses some energy during the scattering process. This loss increases with increasing scattering angle and also causes loss of coherence. The inelastic scattering depends on the Klein-Nishina (KN) formula.[47,48]

$$K_{\mathrm{KN},s}(\gamma,\theta) = \left(1+\frac{\gamma^2[1-\cos(\theta)]^2}{[1+\cos^2(\theta)]\{1+\gamma[1-\cos(\theta)]\}}\right)\Bigg/ \{1+\gamma[1-\cos(\theta)]\}^2, \tag{11}$$

K_{KN} enters as a factor in the formula for the incoherent-scattering cross section. The cross section for incoherent scattering is then

$$\frac{d\sigma_{\mathrm{incoh},s}(q,\theta)}{d\Omega} = K_{\mathrm{KN}}(\gamma,\theta)\sum_{i=1}^{M} S_i(q), \tag{12}$$

where $S_i(q)$ can be found in tables[45,46] and are called incoherent-scattering factors or Compton scattering factors for the photon energies considered in this work. $\gamma = h\nu_0/m_e c^2$ is the relativistic term, which ranges between 1% and 2% for the photon energies of interest in this work. Note that it presents the same polarization properties as Rayleigh or Thomson scattering in the limit of photon energies $\ll$0.5 MeV, or more explicitly for nonrelativistic scattering. At highly relativistic energies the polarization properties are lost. The incoherent and coherent differential cross sections can now be defined. In our calculations we set the Klein-Nishina factor, $K_{\mathrm{KN}}(\gamma,\theta)=1$.

The calculations of the cross sections can be simplified considerably if some approximations are done: (1) the scattering is nonrelativistic; (2) the scattering occurs from ensembles of molecules, particles, etc., with a complete random (isotropic) spatial distribution; (3) the electron distribution is mainly centered around the atoms with a distribution similar to that of the corresponding free atoms.

The differential cross section for coherent scattering (in electron units) for a single species can then be described by the Debye formula[38,49] as

$$\frac{d\sigma_{\mathrm{coh},s}(q)}{d\Omega} = \sum_{i=1}^{M}\sum_{j=1}^{M} f_i^*(q) f_j(q)\frac{\sin(q|\bar{r}_i-\bar{r}_j|)}{q|\bar{r}_i-\bar{r}_j|}, \tag{13}$$

where i and j refer to the atomic centers of the species.

The coherent and incoherent number of photons scattered by linearly polarized radiation (s) into the solid angle $d\Omega$ per time unit is now for orthogonally polarized radiation

$$dP_s(q) = {r_e}^2 N\sum_{i}^{M} x_i\left[\frac{d\sigma_s(q)}{d\Omega}\right]_i I_{s0}d\Omega dV. \tag{14}$$

For polarized x-ray radiation at the angle φ relative the plane of scattering the number of photons scattered per unit time into the solid angle $d\Omega$ then becomes

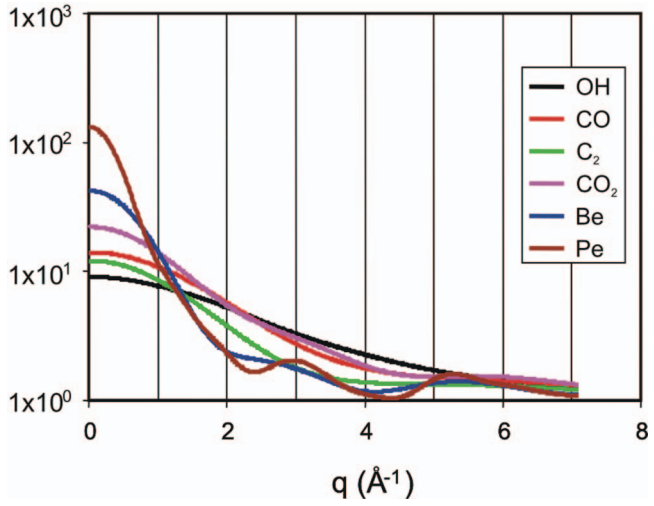

FIG. 1. (Color) Calculated scattering cross sections ($\varphi=90°$; and $\lambda=1.77$ Å) in electronic units divided by N_e: Be=benzene and Pe=perylene.

$$dP[q(\lambda,\theta),\theta,\varphi] = [\sin^2(\varphi)+\cos^2(\varphi)\cos^2(\theta)]r_e{}^2 N \times \sum_i^M x_i \left[\frac{d\sigma_s(q)}{d\Omega}\right]_i I_0 d\Omega dV, \quad (15)$$

where x_i is the mole fraction of species i, N being the total concentration, and dV is the scattering volume element. This equation holds for species in gas phase where the spatial distribution of the different species has a high degree of randomness. *I* condensed phases this assumption holds no longer, since the distribution of the species is relatively ordered.

Multiple scattering effects can be neglected, since the single-scattering process is very weak compared with the scattering in the visible-UV-wavelength region. The real and imaginary parts of the complex refractive index in the x-ray region of interest are very close to 1 and 0, respectively, for instance, for carbon $n=0.999\,991$ and $k=2.025\times10^{-8}$ for $\lambda=1.771$ (7 keV).

MOLECULES AND CARBON STRUCTURES

Calculations were performed on different molecular and nanometric species of different structures that are of interest for combustion. The C–C interatomic distances were set to 1.42 Å for aromatics and nanotubes, and 1.54 Å for diamonds. These values were chosen since they are often found as reference values for graphite (planar bonds, sp^2) and diamond (sp^3), respectively. Bond distances for diatomic species were obtained from different references.[50,51]

The scattering in the forward region $\theta=0°$ ($q=0$ Å^{-1}) is proportional to the total number of electrons squared, N_e^2, of the object. This means that hydrogen atoms scatter only very weakly compared with carbon, nitrogen, and oxygen atoms. Figure 1 shows an example of scattering patterns for different molecular species. The scattering cross sections reported in the figure were first calculated in units of electrons, i.e., according to Eqs. (12) and (13) and then normalized on their number of electrons N_e. The scattering in the forward direction in these plots is seen to increase with the size of species. The chosen normalization procedure of the cross sections is useful when one considers changes in the scattering properties caused by chemical and structural changes within a confined and isolated volume. In a reaction vessel the total number of atomic species or the total number of electrons is maintained constant. If we, for example, consider the conversion of ethylene to benzene (C_6H_6), according to the stoichiometric relation: $3C_2H_4 \rightarrow 1C_6H_6+3H_2$ the corresponding changes in cross sections would be: $3\times16^2 \rightarrow 42^2+3\times2^2$ and the scattering would increase by a factor 2.3.

The scattering in the wide-angle region on the other hand behaves differently. Although changes in the scattering intensity with the respect to N_e are marginal at very large angles such as $\theta=180°$ ($q=7.1$ Å^{-1}, $\lambda=1.77$ Å), features related to the structure of the species start to appear as N_e is increased. This can be seen by comparing the patterns for benzene and the PAH perylene ($C_{20}H_{10}$).

We have seen that on one hand the scattering region in the low q region ($q<1$ Å^{-1}, $\theta=16.2°$ at 1.77 Å) is useful for evaluating molecule and particle size as well as size distributions.[32,33] This is the region to which SAXS measurements generally are confined. On the other hand, the complementary region ($q>1$ Å^{-1}) contains most of the information on molecular or particle structure as we will show. Below we will analyze the wide-angle scattering region for different species in more detail.

The size- and structure-dependent properties of the scattering become more evident in Fig. 2, where a larger selection of species is shown for comparison. Note that the scattering cross sections have been rescaled so that the patterns of the different species are more easily compared on a logarithmic scale. The following types of species have been plotted: (1) diatomic species, (2) planar aromatic substances from benzene to graphene, (3) curved aromatic structures obtained from half fullerene spheres, (4) nanotubes as cylindrical aromatic species, (5) graphite structures of different size and shapes, (6) diamond structures of different size and shape, (7) homogeneous spherical shell-like structures, (8) fullerenes, (9) onionlike structures consisting of concentric homogeneous shells with two and three layers, and (10) onions of concentric fullerene molecules. To the right of graph we list the relevant properties different species: structure, size, number of carbon atoms, and symmetry or shape.

The species containing almost exclusively aromatic units given by hexagonal and/or pentagonal rings of carbon atoms, i.e., species of types (2), (3), (4), (5), (8), and (10) show local maxima in similar regions. The local maxima for diamonds (6) occur in the same regions, however, the structure around $q=3$ Å^{-1} is more symmetric, whereas the "aromatic" species present a less symmetric feature weighted towards slightly larger q values. The differences become stronger for the second maximum region for $q>5$ Å^{-1}. In this region the shift of the aromatic species becomes clearer. Graphite (5) shows an additional feature in the region $1.5\ \text{Å}^{-1}<q<2.0$ Å^{-1}, which is related to the stacking of the graphene sheets (planar sheets consisting of a hexagonal structure with a C–C bond distance of 1.42 Å) or PAH sheets into graphite. One observes that this maximum becomes sharper and shifts to-

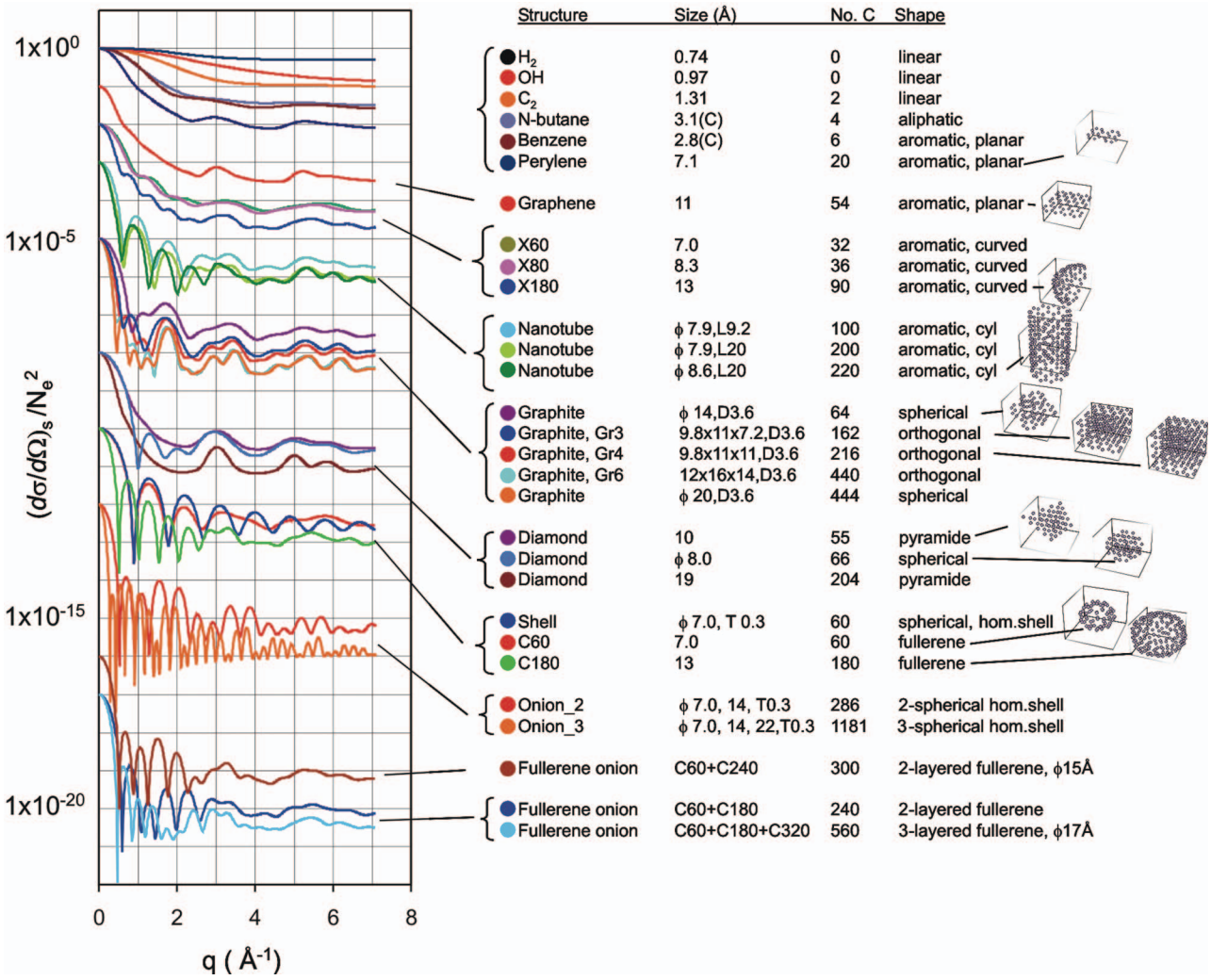

FIG. 2. (Color) Calculated scattering cross sections normalized against N_e^2 calculated for different structures ($\varphi=90°$; $\lambda=1.77$ Å). On the right of the scattering plots, the length (L), and the diameter (Φ) of the carbon structures are given. For spherically homogeneous shells and onions, the shell thickness (T) was set to 0.3 Å. The interlayer distance (D) for graphite structures was set to 3.6 Å. The cross sections have been rescaled so that the variations are readily seen within a group of structure. The given sizes for n-butane, naphthalene, and perylene refer to the size of the carbon structure (C). The lengths of the axes in the graphic representation of the structures are 1 nm.

wards higher q values as the number of layers is increased. The effect of narrowing with increasing size is observed also for the aromatic structure. The interlayer distance for graphite particles in these calculations was set to 3.6 Å which is slightly larger than for "perfect" graphite, 3.4 Å. In soot analysis the interlayer distance is frequently found to be larger than 3.4 Å. Values of 3.6 Å are often found, however, values of 4.0 Å or even higher have been reported (see Refs. 52 and 53 and references therein).

Many of the curves present strong oscillations. The intensity of these oscillations is strongly correlated to the symmetry of the species. The different symmetries in order of decreasing amplitude of the oscillations are (A) spherical homogeneous shells, (B) fullerenes, (C) cylindrical structures and nanotubes, and (D) circular curved surfacelike structures such as half fullerenes.

For the calculations of cross sections of homogeneous spherical shell-like and onionlike structures, a Lorenz-Mie code was modified for applications valid under the Rayleigh-Gans criterion of scattering given by Van de Hulst.[41] The Lorenz-Mie theory[54,55] describes the elastically scattered radiation in the far field for spherical, homogeneous, and isotropic objects. We first calculated the complex amplitudes of scattering for shells (diameter D) by subtracting the complex amplitude for a smaller homogeneous sphere, $D-\delta/2$ Å, from that for the larger homogeneous sphere, $D+\delta/2$ Å, where δ is the thickness of the shell. The complex amplitudes for onions were then obtained by adding the complex amplitudes for the shells of the respective diameters. The typical shell thickness chosen was $\delta=0.3$ Å. The square absolute of the complex amplitudes for the shells and onions were then calculated, yielding the corresponding cross sections. The value of the cross section was calibrated by assigning the scattering cross section of the C_{60} molecule to the shell of the same diameter ($D=7.0$ Å, $\delta=0.3$ Å). The cross sections of the other shells and of the onions were then scaled as the square of the corresponding ratios between their volumes and that of the C_{60} equivalent shell.

The spherical shells present almost periodic oscillations with a frequency $q_D^{-1}=D/6.3$ Å, where D is the diameter of

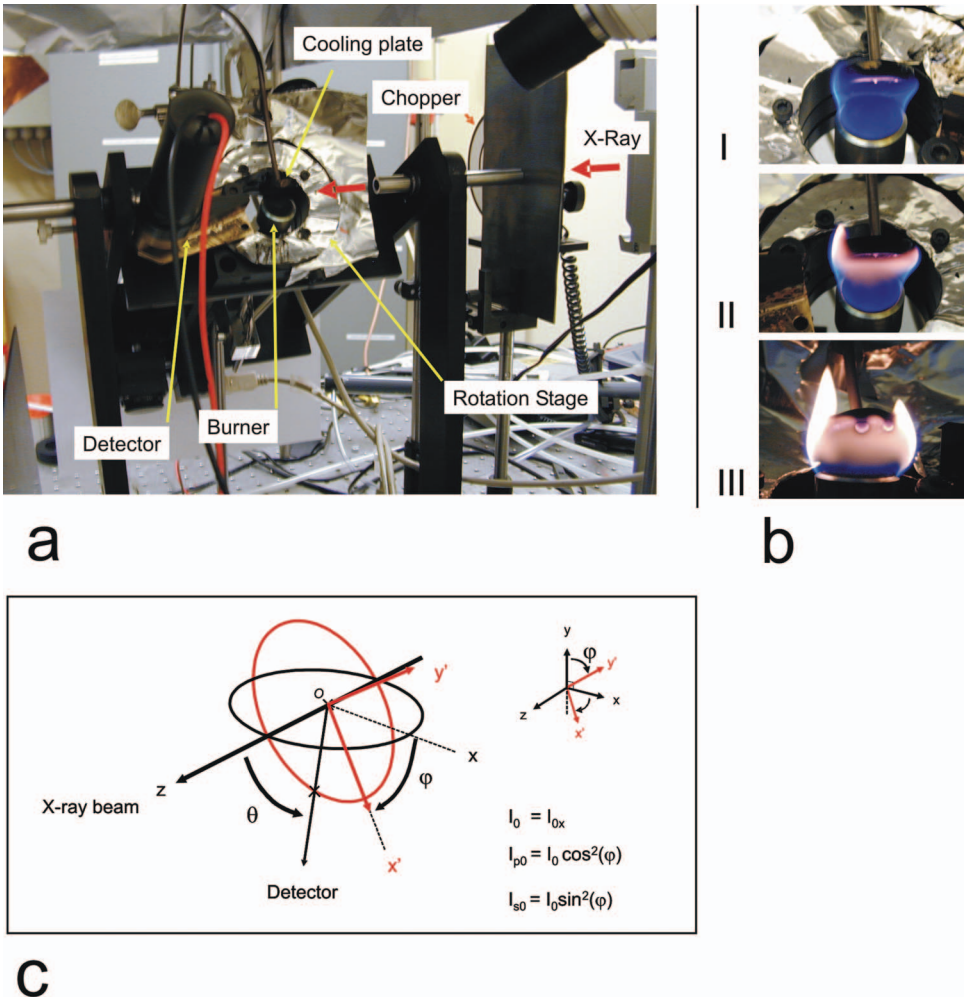

FIG. 3. (Color) (a) Left picture showing the main parts of the experimental setup in the x-ray hutch of beamline D 611, MAX-Lab, Lund. (b) The series of pictures on the right show flames of ethylene for different C/O ratios at the point of injection: (I) C/O=0.9, (II) C/O=4.9, and (III) C/O=∞. (c) The polarization of the x-ray beam (irradiance I_0) is mainly in the horizontal plane (z,x) in the direction of the x axis. In order to increase the signal at wide scattering angles the scattering plane defined by (z,x') was rotated the angle $\varphi=60°$ around the z axis. The orthogonal and parallel polarized components relative to the scattering plane then are according to Eq. (4) $I_{s0}=I_0 \sin^2(\varphi)$ and $I_{p0}=I_0 \cos^2(\varphi)$, respectively.

the shell. The oscillatory property of the structure is strongest for spherical structures, but clearly present also for cylindrical structures. The frequency of this structure is approximately proportional to the diameter of the shell. This property can be used as a reference to determine shell equivalent size (SES) for oscillations measured in the experimental patterns.

The ability to distinguish particles from their shape and "lattice" structure can be exemplified by comparing the cross sections of species in the following two examples we have chosen based on Fig. 2: (I) the homogeneous spherical shell, $D=7.0$ Å, and the fullerene C_{60}; (II) the homogeneous onionlike shell system onion 2 and the fullerene onion $C_{60}+C_{240}$. One observes that the two species in each example present oscillations which are related to the shape in the region $0\ \text{Å}^{-1}<q<2.5\ \text{Å}^{-1}$, whereas the lattice structure becomes evident for q values outside this region. Consequently SAXS measurements may provide information on the shape of these particles, but fail to provide information of the lattice structure, which in this case is of aromatic nature. Thus WAXS measurements become indispensable for the determination of the lattice structure.

EXPERIMENTS AND PROCEDURES

The setup

The main parts of the experimental setup have been described in an earlier publication.[35] We now give a short description focusing on differences from the previous work. Figure 3(a) shows a picture taken for the setup, where the main parts are reproduced. In all measurements the azimuth angle φ was 60°. Different types of flames are shown in Fig 3(b). The experimental results reported below refer to nonpremixed flames.

The incoming photon flux used in the experiments was typically $2\times10^{10}\ \text{s}^{-1}$ at a photon energy of 8 keV (1.55 Å). The plane of the polarization was horizontal. The relative bandwidth $(\Delta\lambda/\lambda)$ was 2×10^{-4}. The x-ray radiation was focused by a grazing incidence mirror upstream the monochromator. The diameter of the focused radiation was 2×10^{-2} cm, yielding an irradiance of 6×10^{14} photons $\text{s}^{-1}\ \text{cm}^{-2}$. The detector for the scattering measurements consisted of a scintillator/photomultipler unit (ZnS, Ag/Hamamatsu H6533) mounted on a rotation stage. The aperture of the detector was determined by two rectangular slits,

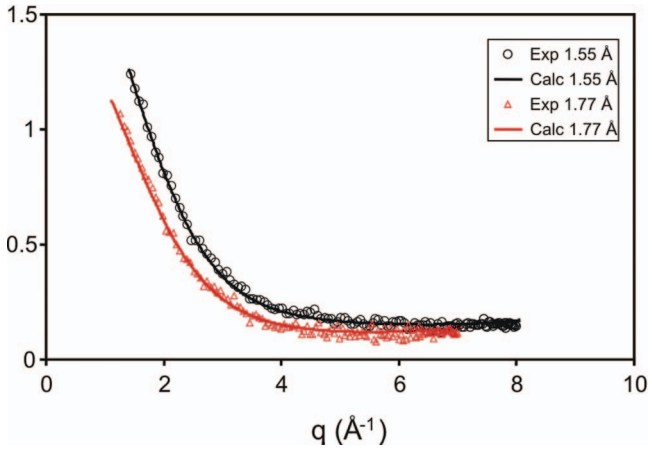

FIG. 4. (Color) Measured and calculated scattering patterns for room air, $\varphi=60°$.

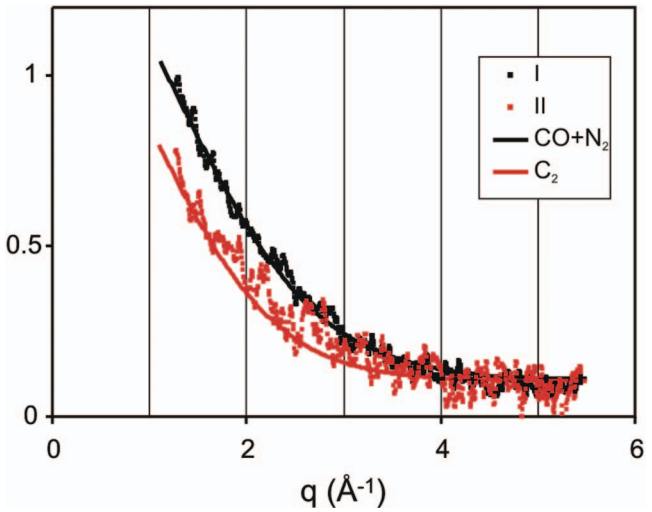

FIG. 5. (Color) Scattering patterns measured for a flame at two different conditions: (I) gas velocity 4.3 cm/s and the C/O ratio=1, and (II) 0.94 cm/s and C/O=∞. The calculated values are for the expected composition of CO and N_2 for condition (I) and C_2 for (II); $\varphi=60°$ and $\lambda=1.77$ Å.

2 mm wide and 20 mm high each, at 30 and 75 mm from the center of rotation (the center of the measured volume), respectively.

The measurements were performed with a time constant of 3 s on the lock-in amplifier. The frequency of the chopper was 347 Hz. The scattering patterns were typically recorded between 157° and 10° scattering with a step of 0.2°. The acquisition time of a scan was 7 min. The angular scans were performed in the backward angular direction, i.e., starting from the largest scattering angle of the scan. Due to the rectangular shape of aperture of the detector, the effective lateral or angular resolution was a function of the scattering angle. The effective scattering angle observed by the detection system became slightly distorted as the detector position was deviated from $\theta=90°$. The effect of the angular distortion and changing resolution was included in the calculations of theoretical scattering patterns to be used for comparisons with measured scattering patterns.

The detector was calibrated into volts/photons, measuring the transmitted radiation through a 300-μm-thick Cu foil. Afterwards, the intensity scattered from room air was measured then at $\theta=50°$ and 8 keV. About 2×10^4 photons s^{-1} were scattered into the detection system. In all the experiments, the intensity of the measured signal was normalized with respect to the scattering volume. The scattering volume was approximated as proportional to the depth of the measured volume. This depth was set as proportional to $1/\sin(\theta)$ in the angular region of the measurements. The concentration was obtained from the perfect gas law at 298 K and 1 atm pressure.

In order to ensure that the measurement procedures were correct scattering patterns were measured for two different radiation wavelengths, 1.55 and 1.77 Å. The measured patterns were normalized for the scattering volume. The measured patterns were then compared with calculated patterns for $\varphi=60°$. Figure 4 shows the measured patterns recorded for room air at the two different wavelengths. The normalized patterns fit very well to the calculated patterns. This assured us to proceed with the flame measurements.

Flame measurements

Measurements were performed on flames for different mixtures of ethylene and air. Some different types of flames are shown in the pictures of Fig. 3(b). The burner was small, 20 mm in diameter and not cooled. Above the burner a flame-stabilizing metal plate was placed. The plate also worked as a heat sink. For the same feeding conditions (feeding rate and mixture ratio between fuel and air, specified as the total C-atom to O-atom ratio, C/O) the constitution of the flame changed from the time of ignition until the burner temperature stabilized. The flames became less luminous and less sooty as the temperature increased due to the increased entrainment of hot surrounding air. Before any measurements started we waited until the flame had stabilized for sure. The pictures show the flames for the stabilized burner temperatures.

In order to test the setup for different flame conditions measurements were performed for a "blue" oxygen-rich flame and a "yellow" oxygen-deprived nonpremixed flame. Figure 5 shows the measured scattering patterns for the two different flame conditions: the blue flame [C/O=1, picture (I) in Fig. 3(b)] and the other yellow flame where the air flow was closed [C/O=∞, picture (III) in Fig. 3(b)]. In the same graphs calculated scattering patterns have been inserted. For the blue flame (C/O=1) the calculated pattern was obtained for a mixture of CO and N_2 expected from the combustion of ethylene and air mixed for C/O=1. For the yellow flame when no air was supplied to the burner the species used in the calculations was C_2. The agreement between the measured and the calculated patterns is very good. The results agree with the expected main configurations of carbon containing molecules for the different conditions. One also notices that signal fluctuates more in the yellow flame. The larger fluctuations in this flame were caused by a combination of increased density variations in the flow field and the broader spectrum of species composition expected for rich flame conditions.

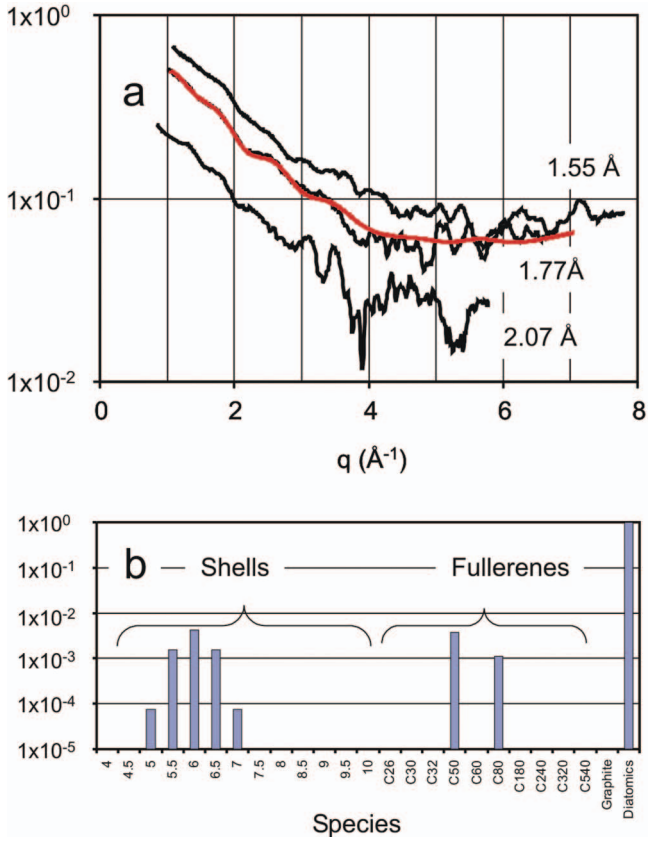

FIG. 6. (Color) (a) Measured scattering patterns $\varphi=60°$ for different radiation wavelengths plotted as a function of q. The red curve is a fit from scattering calculations. (b) The relative species concentrations used from the calculated curve in (a). The numbers 4–10 on the abscissa represent the diameter of the spherical shells.

Figure 6 shows results from measurements on a nonpremixed ethylene flame operating at the fuel rate 1.4 cm s^{-1}. The flame was luminous, but did not produce significant soot growth on the flame-stabilizing plate. Scattering patterns were measured at different wavelengths for the same flame conditions. Despite the total measurement time of approximately 30 min the flame was considerably stable. The scattering patterns obtained from this series of measurements at different wavelengths show that the scattering features are maintained since the patterns are similar when they are plotted as a function of q (the validity of such a plotting procedure was demonstrated by Ossler and Larsson[35]). The experimental data were then compared with calculated scattering patterns for different weights of species. The red curve in Fig. 6(a) is a fit for $\lambda=1.77$ Å. Figure 6(b) shows the composition of species used in the fit. Shell-like structures with the diameter around 6 Å and fullerenes smaller than 1 nm in diameter seem to dominate the structural content of the patterns.

The measured intensity of the scattered radiation decreases strongly with increasing scattering angle. In order to evidence the structural information contained in the measured patterns, in particular, in the smaller angular region, the experimental and the calculated data were subtracted by the exponential function $\exp(-\theta/17)$. The exponential constant was chosen to yield a resulting plot with close to a constant baseline in a broad range of q values. Curve (I) in Fig. 7(a) shows the data corresponding to Fig. 6 when the data were subtracted by $1.2\exp(-\theta/17)$. Curves (II)–(V) are experimental curves obtained from nonpremixed ethylene flames in another series of measurements. These data are

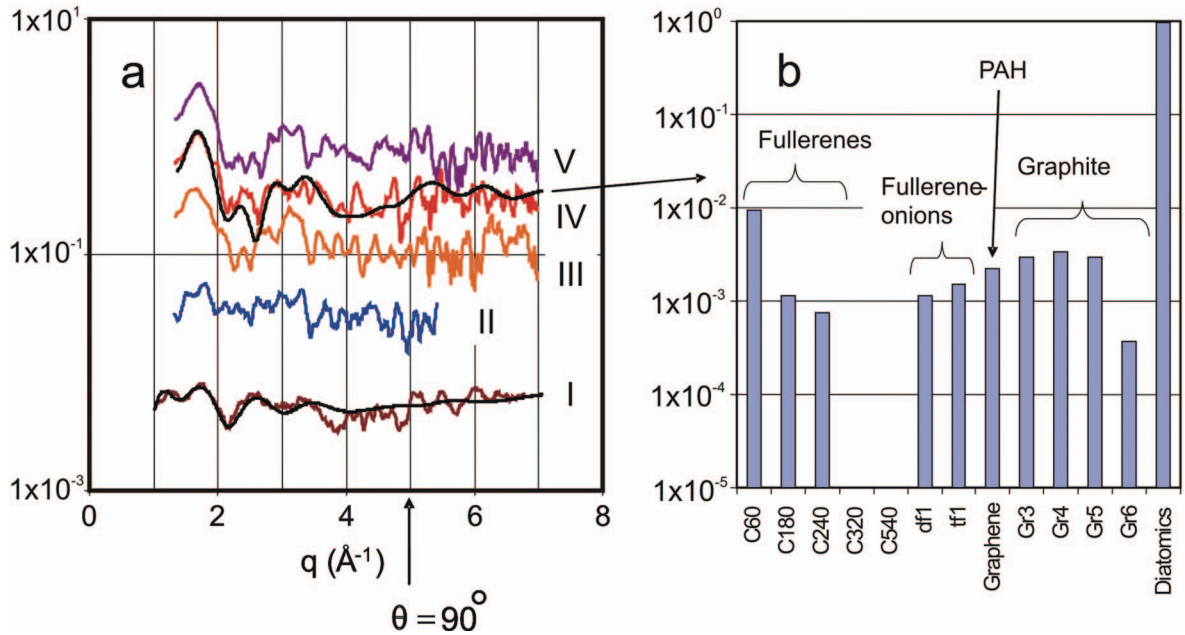

FIG. 7. (Color) (a) Plots of experimental (colored) and calculated (black) scattering patterns obtained from different measurements ($\varphi=60°$ and $\lambda=1.77$ Å). The measured and calculated intensities were subtracted by the function $\exp(-\theta/17)$ in order to evidence the structure of the patterns (I)–(V). The fit for curve (I) is the same as reported in Fig. 6, while the fit for curve (IV) was obtained for the composition given in (b). Curve (II) is a measurement at a lower feeding rate (0.94 cm s^{-1}), whereas curves (III)–(V) were obtained for an increased feeding (1.4 cm s^{-1}) rate so that the soot formed readily on the cooling plate. In (b) df1 and tf1 stand for the fullerene onions, $C_{60}+C_{180}$ and $C_{60}+C_{180}+C_{320}$, respectively. Gr3 and Gr4 represent three- and four-layered graphene sheets, respectively, with 54 carbon atoms each. Gr5 is a four-layered graphite particle with 88 carbon atoms in each sheet. Gr6 is the same as Gr5 but with an additional sheet. df1 and tf1 are the last two- and three-layered fullerene onions given in Fig. 2.

subtracted by $2.5\exp(-\theta/17)$. Note that different scales have been used for the plots given in order to simplify the comparison between them. The scales used in the plots are (I) 1.0, (II) 5.0, (III) 5.0, (IV) 12, and (V) 30. The data were obtained for different flow- and particle-producing conditions inside the flame. Curves (II)–(V) were obtained from a continuous series of measurements and are given in the order they were measured. Going from curve (II) to (III) when the flow rate was increased from 0.9 to 1.4 cm s^{-1}, the patterns are seen to change drastically. For the higher flow rate, Curves (III)–(V) show signatures of nanometer-sized graphite particles with an interlayer distance of 3.6 Å, in the region $1.5\ \text{Å}^{-1} < q < 2\ \text{Å}^{-1}$. The noises in these curves seem to be stronger than for curve (II). This might be an indication that there are temporal fluctuations of species concentrations between nanoparticles and smaller molecules. One also observes that the peak due to graphite slightly moves towards larger q values with increasing curve number. Such an effect is expected when the number of layers in graphite increases, e.g., from 2 to 3 or 3 to 4, or when the interlayer distance between the graphene sheets decreases by cooling. The fit of curve (IV) shows that the composition given by Fig. 7(b) contains considerable amount of spherical structures such as fullerenes and fullerenelike onions. However, the interpretation of the fullerenelike onions is still preliminary. In any case the graphite particle content in the scattering patterns is strongly present for curves (III)–(V) whereas they seem to be almost absent in curve (I). In fact the fit of curve (I) was obtained without including graphitelike species.

DISCUSSION

Our measurements give insights in the early stage of the nanoparticle/soot formation processes and the role of fullerenes and graphitelike nanoparticles. The measurements rely on *in situ* detection of the scattered x-ray radiation and the quantitative interpretation of the scattering signal based on the comparison with scattering calculations. In the calculations atomic configurations of electron clouds were used. These configurations are inherently defined in the tabulated values for coherent and incoherent atomic form factors, which consequently do not describe the exact electron-density distribution of the electrons of the different molecules. Nevertheless, the correspondence between measured and calculated scattering patterns was very good.

The production of soot on the flame-stabilizing cooling plate appeared under the presence of nanometer-sized graphite particles in the flame. These flames showed also the presence of fullerenes and possibly fullerenelike onions. A much lower tendency to soot production was instead observed in flames rich on fullerenes or spherical structures but poor on graphite particles. The temperature obtained from these measurements was higher than for the soot producing regions.

The nanometer-sized graphitelike particles may arise either from the condensation of graphene sheets or PAH of predominantly hexagonal structure. The fits used for the soot producing conditions included the contribution from fullerenes, planar PAH or graphene structures, and nanometer-sized particles with different numbers of layers between 2 and 4. The curved PAHs were not included in the fits, since the level of signal to noise of the measurements did not require their contribution, however, they might very well have been present in reality. In our fits they would most probably be included in the PAH or fullerene concentrations used in the calculations of the fitting scattering patterns.

Fully developed soot particles typically consist of fractal-like clusters of almost spherical-like units, so-called primary soot particles, with a diameter typically around 20 nm. These primary soot particles of soot from atmospheric-pressure premixed ethylene/air flames, reported by Grieco *et al.*,[10] have shown to contain curved layers in the HRTEM images that according to the researchers were indicative of fullerenes. Images on soot particles from carbon black furnaces by Pontier Johnson *et al.*[56] also showed fullerenelike structures incorporated in the soot particles. In our measurements, HRTEM images on soot particles collected from the cooling plate showed similar results.

The fitting of our experimental x-ray scattering data on flames was based on the assumption of what major components could be present. These components included the structures observed from electron-microscopy imaging given in, e.g., Refs. 9–12 The structures observed in our experimental x-ray scattering patterns were then identified by comparing them with the structures of the theoretical patterns in Fig. 2. For instance, the main x-ray scattering features found for curve (IV) in Fig. 7 such as the broadened peak at $q = 1.75\ \text{Å}^{-1}$ were attributed to graphitelike structures. However, fullerenes and fullerene onions had to be added to improve or reconstruct different features. These species were needed to increase the intensity for $q < 1.5\ \text{Å}^{-1}$, decrease the intensity of the "graphite peak" at $q = 1.75\ \text{Å}^{-1}$, reconstruct the feature at $q = 2.3\ \text{Å}^{-1}$, and improve the structure in the region $2.5\ \text{Å}^{-1} < q < 3.5\ \text{Å}^{-1}$.

Consequently, Fullerenes play an important role for the description and formation of soot particles. The primary soot particles may arise from the condensation of fullerenes, together with PAH-like planar or curved aromatic structures and nanometer-sized particles showing more caged or graphitelike structures. These clusters of nanometer-sized particles and molecules may undergo further transformation leading to an increased degree of graphitization of the clustered material.

Fullerenes at low ambient pressure are known to experience phase transitions through sublimation.[57] Figure 8 shows sublimation lines (broken) for different temperatures as a function of fullerene size. These curves were obtained by interpolating and extrapolating the thermodynamic data on sublimation by Markov *et al.*[57] and then calculating vapor pressures for different temperatures as a function of the number of carbon atoms in the fullerene.

Due to the high temperatures during combustion (1400–1800 K) fullerene concentrations may be high before any sublimation into the condensed phase occurs. However, as the fullerene-rich flame gases cool down slowly, progressively the fullerenes condense into particles, which in turn may undergo transformations to more graphitelike structures under still relatively high temperatures. From the previous measurements[35] temperatures were evaluated from the inten-

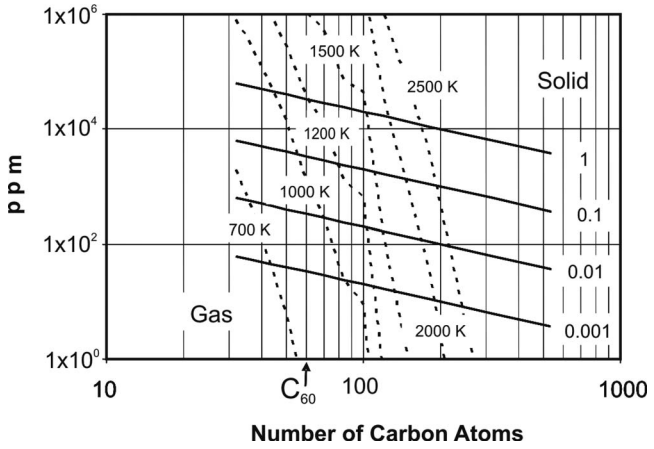

FIG. 8. Conversion factors (full lines) and sublimation curves (broken). The conversion factors for the formation of monodisperse fullerene molecules from the fuel (ethylene) are plotted as a function of the number of carbon atoms in the fullerene molecule. The conversion factors are 1, 0.1, 0.01, and, 0.001. The sublimation curves are plotted as concentration (ppm) for monodisperse fullerenes against the number of carbon atoms. The curves are plotted for different temperatures. The sublimation curves were obtained from values interpolated and extrapolated from the thermodynamic data given Markov *et al.* (see Ref. 57).

sity of the scattering signals. It was found that graphitic nanoparticle formation occurred between 900 and 1000 K. The range of temperature where fullerenelike signatures were found was higher, between 1200 and 1700 K. However, these temperatures should be seen as preliminary results from observations of structural changes in the first sets of measurements. More studies are needed to provide thermodynamic data for particle dynamics under combustion conditions.

In order to evaluate the possibilities of obtaining high concentrations of fullerenes at flame conditions, we wished to compare the thermodynamic data from above with the concentrations that would be expected for different degrees of efficiency in the conversion from the ethylene fuel to fullerenes of a particular size. Figure 8 shows the concentrations in ppm as a function of the number of carbon atoms of the fullerene molecule. The straight lines (full) in Fig. 8 have been plotted for different conversion factors (CFs). These factors correspond to the efficiency for converting X number of C_2 or ethylene molecules into $2C_X$. X stands here for the number of atoms in the fullerene molecule. CF=1 would correspond to converting for example 30 C_2 clusters into 1 C_{60} molecule, CF=0.1 would require 300 C_2 clusters to obtain 1 C_{60}, etc. The results from the experiments and the sublimation data derived from literature[57] show that high concentrations of uncondensed fullerenelike structures are possible to obtain under rich particle producing conditions of combustion at high temperatures.

The accuracy and precision of experimental results can be estimated from the sensitivity of the fits given in Fig. 7: changing the individual species concentrations a factor of 2 gave visible deviations in the fits. In terms of groups of species, i.e., fullerenes and fullerene onions on one hand and PAH and graphite on the other, the relative changes were 0.3.

CONCLUSION

X-ray scattering calculations were performed for a number of species of particular structures and shapes of interest for combustion taking into account the polarization properties of the radiation. The scattering patterns were analyzed, allowing the identification of signatures for molecule and particle structure and symmetry to be used for the analysis of the experimental data. X-ray scattering patterns were then measured *in situ* for air and flames for different conditions of combustion. The experimental data were analyzed with respect to the theoretically defined signatures. In addition, a more quantitative comparison was done, by fitting theoretical patterns to the experimental data.

The results imply that the atomic form factors can be used with sufficient accuracy for determining the scattering properties of air and flames gases also when these are dominated by diatomic species. The analysis and fit of the experimental data showed that high concentrations of spherical or fullerene structures or nanometer-sized graphitelike structures were obtained in the flame depending on the burning conditions. The graphiticlike structures became more evident at lower temperatures in the flame.

The x-ray scattering technique allows *in situ* measurements on atmospheric-pressure flames under rich nanoparticle-producing conditions. For instance, it can be used to study the detailed role of, e.g., fullerenes and nanometer-sized graphitelike particles for the production of soot and give a deeper understanding of the dynamics and mechanisms involved in soot formation processes.

The wide-angle x-ray scattering region has provided useful information on the structure and symmetry of the species during nanoparticle production. This information would be hard to obtain from measurements based only on the forward scattering region. The WAXS technique will thus become a useful complement to the SAXS techniques demonstrated by other groups for measurements of the size distribution. These techniques together will allow a deeper study of molecular and particle dynamics in flames and other gas-phase reactive systems where particles are formed.

ACKNOWLEDGMENTS

We acknowledge Ola Synnergren for beamline support and Professor Reine Wallenberg for performing the HRTEM measurements. The support from Carl Tryggers Stiftelse, Crafoordska stiftelsen, the Swedish Research Council, and the Swedish Foundation for Strategic Research, and the Competence Centre for Combustion is gratefully acknowledged.

[1] A. W. Jensen, S. R. Wilson, and D. I. Schuster, Bioorg Med. Chem. **4**, 767 (1996).
[2] G. Oberdörster, Z. Sharp, W. Kreyling, C. Cox, V. Atudorei, A. Elder, and R. Gelein, Inhalation Toxicol. **16**, 437 (2004).
[3] A. R. Molinelli, M. C. Madden, J. K. McGee, J. G. Stonehuerner, and A. J. Ghio, Inhalation Toxicol. **14**, 1069 (2002).
[4] P. H. M. Hoet, I. Brüske-Hohfeld, and O. V. Salata, J. of Nanobiotechnology. 2:12 (2004).
[5] L. A. Sgro, G. Basile, A. C. Barone, A. D'Anna, P. Minutolo, A. Borghese, and A. D'Alessio, Chemosphere **51**, 1079 (2003).
[6] H.-H. Grotheer, H. Pokorny, H. Barth, K.-L. Thierly, and M. Aigner,

Chemosphere **57**, 1335 (2004).
[7]R. A. Dobbins, G. J. Govatzidakis, W. Lu, A. F. Schwartzman, and R. A. Fletcher, Combust. Sci. Technol. **121**, 103 (1996).
[8]F. Le Normand, L. Constant, G. Ehret, M. Romeo, A. Charai, W. Saikaly, and C. Speisser, Philos. Mag. A **79**, 1739 (1999).
[9]W. Zhu, D. E. Miser, W. G. Chan, and M. R. Hajaligol, Carbon **42**, 1463 (2004).
[10]W. J. Grieco, J. B. Howard, L. C. Rainey, and J. B. Vander Sande, Carbon **38**, 597 (2000).
[11]A. Goel, P. Hebgen, J. B. Vander Sande, and J. B. Howard, Carbon **40**, 177 (2002).
[12]T. H. Lee, N. Yao, T. J. Chen, and W. K. Hsu, Carbon **40**, 2263 (2002).
[13]P. Weilmünster, A. Keller, and K.-H. Homann, Combust. Flame **116**, 62 (1998).
[14]M. Kalberer *et al.*, Science **303**, 1659 (2004).
[15]F. Fugaciu, H. Hermann, and G. Seifert, Phys. Rev. B **60**, 10711 (1999).
[16]H. Hermann, F. Fugaciu, and G. Seifert, Appl. Phys. Lett. **79**, 63 (2001).
[17]A. I. Melker, S. N. Romanov, and D. A. Kornilov, Materials Physics and Mechanics 2, 42 (2000).
[18]T. Metz, X. Bai, F. Ossler, and M. Aldén, Spectrochim. Acta, Part A **60**, 1043 (2004).
[19]F. Ossler and M. Aldén, Appl. Phys. B: Lasers Opt. **64**, 493 (1997).
[20]N. A. Borisevich, *Vozbuzhdenye sostoyanya slozhnykh molekul v gazovoy faze* (*Excited States of Complex Molecules in the Gas Phase*) (in Russian) (Nauka y Tekhnika, Minsk, 1967).
[21]F. Ossler, T. Metz, and M. Aldén, Appl. Phys. B: Lasers Opt. **72**, 465 (2001).
[22]F. Ossler, T. Metz, and M. Aldén, Appl. Phys. B: Lasers Opt. **72**, 479 (2001).
[23]A. Leipertz, F. Ossler, and M. Aldén, in *Applied Combustion Diagnostics*, Polycyclic Aromatic Hydrocarbons and Soot Diagnostics by Optical Techniques edited by K. Kohse-Höinghaus and J. B. Jeffries (Taylor & Francis, New York, 2002).
[24]T. Ni and L. A. Melton, Appl. Spectrosc. **47**, 773 (1993).
[25]T. Ni and L. A. Melton, Appl. Spectrosc. **50**, 1112 (1996).
[26]S. A. Kaiser and M. B. Long, Proc. Combust. Inst. **30**, 1555 (2005).
[27]P. Minutolo, G. Gambi, and A. D'Alessio, Twenty-Seventh Symposium (International) on Combustion, The Combustion Institute, 1461 (1998).
[28]L. A. Sgro, P. Minutolo, G. Basile, and A. D'Alessio, Chemosphere **42**, 671 (2001).
[29]L. A. Melton, Appl. Opt. **23**, 2201 (1984).
[30]S. Will, S. Schraml, and A. Leipertz, Appl. Opt. **37**, 5647 (1998).
[31]C. Schoemaecker Moreau, E. Therssen, X. Mercier, J. F. Pauwels, and P. Desgroux, Appl. Phys. B: Lasers Opt. **78**, 485 (2004).
[32]W. A. England, Combust. Sci. Technol. **46**, 83 (1986).
[33]J. P. Hessler, S. Seifert, and R. E. Winans, Proc. Combust. Inst. **29**, 2743 (2002).
[34]G. Beaucage, H. K. Kammler, R. Mueller, R. Strobel, N. Agashe, S. E. Pratsinis, and T. Narayan, Nat. Mater. **3**, 370 (2004).
[35]F. Ossler and J. Larsson, Chem. Phys. Lett. **387**, 367 (2004).
[36]J. B. A. Mitchell, C. Reibrion-Roe, J.-L. Legerrec, G. Taupier, N. Huby, and M. Wulff, Combust. Flame **131**, 308 (2002).
[37]H. Wang, B. Zhao, B. Wyslouzil, and K. Streletzky, Proc. Combust. Inst. **29**, 2749 (2002).
[38]A. Guinier, *X-ray Diffraction: In Crystals, Imperfect Crystals, and Amorphous Bodies* (Dover, New York, 1963).
[39]B. E. Warren, *X-ray Diffraction* (Dover, Toronto, 1990).
[40]L. V. Azároff, R. Kaplow, N. Kato, R. J. Weiss, A. J. C. Wilson, and R. A. Young, *X-ray Diffraction* (McGraw-Hill, New York, 1974).
[41]H. C. Van de Hulst, *Light Scattering by Small Particles* (Dover, New York, 1981).
[42]M. Kerker, *The Scattering of Light and Other Electromagnetic Radiation* (Academic, New York, 1969).
[43]C. F. Bohren and D. R. Huffman, *Absorption and Scattering by Small Particles* (Wiley, New York, 1983).
[44]NIST Database, *Tables of X-ray Mass Attenuation Coefficients and Mass Energy Absorption Coefficients*.
[45]E. Warren, *X-ray Diffraction*, Reprinted Tables of International Tables for X-ray Crystallography Vol. III.B (Dover, Toronto, 1990).
[46]J. H. Hubbel, W. J. Weigle, E. A. Briggs, R. T. Brown, D. T. Cromer, and R. J. Howerton, J. Phys. Chem. Ref. Data **4**, 471 (1975).
[47]O. Klein and Y. Nishina, Z. Phys. **52**, 853 (1929).
[48]W. Heitler, *The Quantum Theory of Radiation* (Clarendon, London, 1954).
[49]P. Debye, Ann. Phys. **46**, 809 (1915).
[50]NIST Database, Chemistry WebBook, Physical Reference Data N. 69, *Constants of Diatomic Molecules*.
[51]*Handbook of Chemistry and Physics*, edited by D. R. Lide, 75th ed. (CRC, Boca Raton, FL, 1994).
[52]Á. B. Palotas, L. C. Rainey, C. J. Feldermann, A. F. Sarofim, and J. B. Vander Sande, Microsc. Res. Tech. **33**, 266 (1996).
[53]R. L. Vander Wal, A. J. Tomasek, M. I. Pamphlet, C. D. Taylor, and W. K. Thompson, J. Nanopart. Res. **6**, 555 (2002).
[54]L. V. Lorenz, Vidensk. Selsk. Skr. 6, 1 (1890).
[55]G. Mie, Ann. Phys. (N.Y.) 25, 377 (1908).
[56]M. P. Pontier Johnson, J. B. Donnet, T. K. Wang, C. C. Wang, R. W. Locke, B. E. Brinson, and T. Marriot, Carbon **40**, 189 (2002).
[57]V. Yu. Markov, O. V. Boltalina, and L. N. Sidorov, Russ. J. Phys. Chem. **75**, 1 (2001).